AIP | Journal of Applied Physics

Electron microscope verification of prebreakdown-inducing α-FeSi2 needles in multicrystalline silicon solar cells

A. Hähnel, J. Bauer, H. Blumtritt, O. Breitenstein, D. Lausch et al.

Citation: J. Appl. Phys. **113**, 044505 (2013); doi: 10.1063/1.4779601
View online: http://dx.doi.org/10.1063/1.4779601
View Table of Contents: http://jap.aip.org/resource/1/JAPIAU/v113/i4
Published by the American Institute of Physics.

Electron microscope verification of prebreakdown-inducing α-$FeSi_2$ needles in multicrystalline silicon solar cells

A. Hähnel,[1,a)] J. Bauer,[1] H. Blumtritt,[1] O. Breitenstein,[1] D. Lausch,[2] and W. Kwapil[3]
[1]*Max Planck Institute of Microstructure Physics, Weinberg 2, 06120 Halle (Saale), Germany*
[2]*Fraunhofer Center for Silicon Photovoltaics, Walter-Hülse-Str. 1, 06120 Halle (Saale), Germany*
[3]*FMF University of Freiburg, Stefan-Meier-Str. 21, 79104 Freiburg i. Breisgau, Germany*

(Received 21 September 2012; accepted 2 January 2013; published online 23 January 2013)

It had been shown already earlier by X-ray microanalysis that, in positions of defect-induced junction breakdown in industrial multicrystalline (mc) silicon solar cells, iron-containing precipitates may exist. However, the nature of these precipitates was unknown so far. Here, in such positions, scanning transmission electron microscopy was performed after defect-controlled focused ion beam preparation. First of all, the defect site was localized by microscopic reverse-bias electroluminescence imaging. The high accuracy of following FIB target preparation (<0.1 μm necessary) was obtained by both, electron beam-induced current imaging and secondary electron material contrast observation during the slice-by-slice milling of the TEM specimen. By nano-beam electron diffraction (NBED) and energy dispersive spectroscopy, the iron-containing precipitates were identified as α-type $FeSi_2$ needles, about 30 nm in diameter and several μm in length. The $FeSi_2$ needles show preferential orientation relationships to the silicon matrix and are located in terraced large-angle grain boundaries. Elaborate nano-beam electron diffraction investigation of the $FeSi_2$ revealed orientation relationships of the precipitate to the silicon, which confirm earlier investigations on monocrystalline material. A model explaining the defect-induced breakdown mechanism due to rod-like α-$FeSi_2$ precipitates is presented. © *2013 American Institute of Physics*. [http://dx.doi.org/10.1063/1.4779601]

INTRODUCTION

Junction breakdown in multicrystalline solar cells may lead to hot spots in shaded cells of a module and is, therefore, a serious reliability problem. Three different types of breakdown have been identified so far in this material, which are early breakdown (type-1), caused by Al-particles at the surface,[1] defect-induced breakdown (type-2), occurring at recombination-active grain boundaries (GBs) and caused by impurity precipitates,[2] and avalanche breakdown (type-3), which occurs either at etch pits or at sites of preferred phosphorous diffusion.[3–5] Defect-induced breakdown (type-2) was demonstrated to appear only in grain boundaries with significant dark electroluminescence (EL) contrast,[4,6] indicating a high degree of metal contamination. Thus, iron-containing precipitates were found to lead to type-2 breakdown in such grain boundaries of multicrystalline solar cells.[2] This type of crystal defects, which shows the highest recombination- and breakdown-activity in multicrystalline solar cells, can clearly be distinguished from other defects in multicrystalline material.[7] It correlates with the open circuit voltage of the cells and was later called "type A" defects.[8] It was also shown that the material lying close to the edge of the casting crucible, which is known to be higher Fe contaminated then the inner parts of the ingot,[9] exhibits a high concentration of type-2 pre-breakdown sites.[4]

Iron (Fe) is known to be one of the most common metallic impurities in industrial solar cells made from Bridgeman H-type/VGF multicrystalline (mc) silicon material. It deteriorates the minority carrier lifetime of the material and may degrade the cell efficiency. A major source of iron is the quartz material and the silicon nitride coating of the casting crucibles.[9] Iron contamination was found to increase the recombination activity of extended crystal defects like dislocations and GBs.[10] However, it is not clear yet whether the increased recombination activity of iron-contaminated crystal defects is due to iron precipitates or due to single iron atoms being attracted to the defects. Based on the model of Kveder,[11] it was recently discussed that the recombination activity of grain boundaries is due to single iron atoms.[12]

Until now, only assumptions about the morphology of iron precipitates in mc-Si causing breakdown sites in solar cells were published. Buonassisi *et al.*[13] have found by synchrotron-based microprobe techniques that a large amount of Fe exists in multicrystalline material in form of submicron sized precipitates, which were identified by X-ray absorption microspectroscopy as $FeSi_2$. The type of the silicide could not be established; however, it was found that these precipitates are not spherical-shaped but elongated in growth direction. Based on DLTS results of monocrystalline silicon and phase diagram data, the formation of β- or γ-type $FeSi_2$ is suspected in the early stage of precipitation, whereas β-$FeSi_2$ depicts the thermodynamically stable phase below 915 °C and γ-$FeSi_2$ corresponds to a metastable isomorph to $CoSi_2$.[14] However, large $FeSi_2$ precipitates in silicon have been attributed to spherical β-type $FeSi_2$ or to rod-like α-type

a)Author to whom correspondence should be addressed. E-mail: ah@mpi-halle.mpg.de. Telephone: +49 345 5582 549. Fax: +49 345 5582 557.

$FeSi_2$. The α-type phase, which is thermodynamically stable above 915 °C, was indeed identified in earlier transmission electron microscopy (TEM) investigations on monocrystalline Si transistor structures. Such rod-like α-$FeSi_2$ or α-type Fe precipitates were also reported to lead to pre-breakdown in the transistor structures.[15,16]

In this paper, we present a thorough structural STEM analysis of breakdown causing Fe precipitates in order to find out their crystallographic nature. Several breakdown sites were investigated, in two of them Fe-containing precipitates were found. The first investigated Fe precipitate is the same that was identified by X-ray microanalysis in Ref. 2 at a typical defect-induced type-2 breakdown site of an industrial alkaline texturized mc-Si solar cell. Since X-ray analysis is not able to give any information about the morphology of the iron precipitates, we took exactly the same sample used in Ref. 2 to perform a high-precision FIB preparation for enabling STEM investigations. Later on, these results were confirmed on another similar breakdown site on a different sample, which was not pre-characterized by X-ray analysis.

EXPERIMENTAL

Two alkaline and one acidic texturized solar cell samples were used for our investigations. All three cells were made out of industrial multicrystalline Bridgeman-type silicon material. During crystallization, the solid phase is cooled down very slowly at a rate of about 0.2 K/min. During this time, iron diffuses from the crucible walls into the material and has enough time to form precipitates. It is well known that, due to this mechanism, in the edge region of the ingot, the iron content may be as high as $10^{15}\,cm^{-3}$, whereas in the center of the block, it is typically $10^{14}\,cm^{-3}$. Wafers made from this material were processed to solar cells by the standard industrial procedure. The cells differ only by their texturization type, but were otherwise processed in the same way implying phosphorous diffusion (approximately 2 h at 800 °C) and full-area screen-printed Al back contact formation by firing at about 900 °C for some seconds. The readily processed cells were subjected to the following procedure:

At first, type-2 breakdown sites were identified by EL measurements at a reverse bias of −10 V in comparison to EL at a forward bias of 600 mV and by electron beam induced current (EBIC). Then, microscopic reverse-bias electroluminescence (μ-ReBEL) was performed to optically localize the breakdown sites in the solar cell structure. The next step was to capture the root cause of the breakdown into a specimen, which is translucent for electron beam in an electron microscope, i.e., into a ∼100 nm-thick slice. This highly precise target preparation could be obtained using the electron beam induced current technique as additional information source directly in the FIB ("*in-situ* EBIC," cf., Ref. 17). For that, a self-made EBIC attachment for the FEI Nova Nanolab 600 FIB was employed. Some details of the defect-controlled FIB preparation are given in Sec. "Sample Selection and Preparation."

In order to characterize the structure and chemistry of the target at a nanometer scale, various TEM and STEM investigations were performed. These were TEM, selected area electron diffraction (SAED), high-angle annular dark-field scanning transmission electron microscopy (HAADF), nanobeam electron diffraction (NBED), and energy-dispersive X-ray spectroscopy (EDXS). For these analyses, a probe C_s-corrected FEI TITAN 80-300 microscope was employed, operating at 300 kV. The same instrument was used for the NBED studies, here being aligned in the microprobe STEM mode. By use of a second condenser aperture of 20 μm, a nearly parallel electron beam with a diameter of ∼3 nm can be established. Point by point stepping this ∼3 nm-beam across a region of interest allows to take diffraction patterns at nm-resolution, which can be analyzed as common SAED patterns, and thus elucidate the particular crystallography at high spatial resolution.

SAMPLE SELECTION AND PREPARATION

In this study, type-2 breakdown sites in two alkaline texturized solar cell samples were investigated in detail. Alkaline texturized solar cells are used, because this kind of solar cells has a much flatter surface compared to isotextured (acidic texturization) ones, which allows taking microscopic μ-ReBEL images with very good spatial resolution of the breakdown sites. The first investigated sample, called "sample 1" throughout the text, is an already pre-characterized sample from Ref. 2. The second sample, named "sample 2" in the following, is a sample from a different alkaline textured solar cell. Here, a region close to the wall of the casting crucible was selected, which is known to contain an increased amount of Fe. A third try was done at a randomly chosen isotextured solar cell.

To identify the exact position of the breakdown site in sample 1, it was localized precisely by μ-ReBEL imaging,[18] which is shown in Fig. 1. The inset of Fig. 1 shows the X-ray element mapping done by micro X-ray fluorescence (XRF) revealing the iron distribution in the breakdown position.[2] The

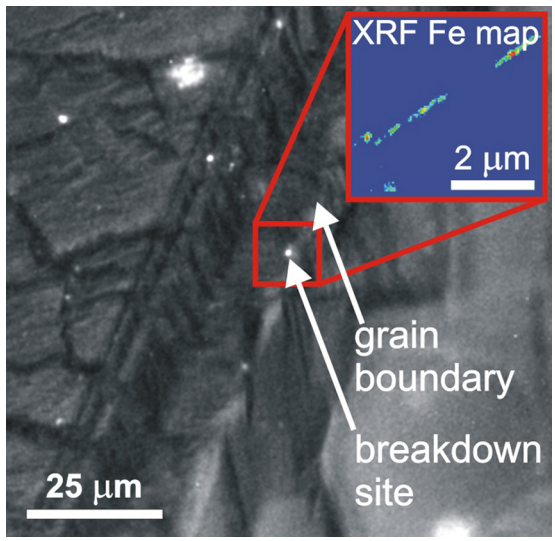

FIG. 1. μ-ReBEL image of the sample from Ref. 2, the inset displays the corresponding μ-XRF map.[2] Inset reprinted with permission from W. Kwapil, Appl. Phys. Lett. **95**, 232113 (2009). Copyright 2009 American Institute of Physics.

optical image in Fig. 1 reveals the grain boundary structure in the vicinity of the breakdown site. By comparing these images with that of Ref. 2, we made sure that we hit exactly the same breakdown site as it was investigated there. The breakdown site is located in a recombination-active grain boundary, which is running nearly perpendicular to the cell surface into the depth. For enabling STEM investigations at the position of this breakdown site, a focused ion beam (FIB) preparation was done nearly parallel to the grain boundary. The goal was to prepare a TEM lamella, which contains the grain boundary including the breakdown site position.

Starting from an initially 5 μm-thick lamella, during the further slice-by-slice thinning, the p-n junction was observed in EBIC. A distinct spike-like deformation of the p-n junction was revealed near to the defect, which allowed to stop the milling process of the front side of the lamella just in the right position, at a distance of several 100 nm from the defect (see, Fig. 2(a)). This spike is caused by an extended defect line, obviously connected to the breakdown site under investigation. On the reverse side of the lamella some μm below the p-n junction, an extended charge-collection contrast feature was found pointing exactly towards the surface-near p-n junction spike on the front side (see, Fig. 2(b)). Possible interpretations of these contrasts will be given later.

After *in-situ* lift-out and transfer of this lamella to a TEM grid, on the reverse side a faint, bright material contrast was observed under optimized secondary electron (SE) imaging conditions, which indicates a rod-like precipitate as shown in Fig. 2(c). This precipitate was cut in a depth of about 5 μm. On further milling this side, the bright contrast showed some fluctuation in strength and shifted towards the position of the EBIC spike on the front side. In a depth of about 2 μm, the contrast disappeared.

Hence a "precipitate line" of more than 5 μm in length is assumed, along which probably precipitates of different thicknesses and lengths are aligned. Slice-by-slice milling in accordance with SE observation finally allowed to prepare a lamella of 400 nm thickness including the GB plane and the precipitate which fully crossed the depth of the lamella under an angle of $\sim 10^\circ$ (see, Fig. 2(d)). This lamella was then studied by STEM, showing the overall geometry of an extended rod of a foreign phase as will be described in detail below. The detailed crystallographic analysis of the precipitate was carried out after a second thinning of the lamella down to about 90 nm, now containing the precipitate in the depth range between 0.7 and 1.3 μm.

To confirm the results found at sample 1, a type-2 breakdown site was localized with μ-ReBEL in sample 2. Here, two breakdown sites appear at a recombination-active GB. Figure 3(a) shows an overlay image of an EL image taken at a forward bias of 601 mV and the μ-ReBEL image taken at -10 V revealing the breakdown site positions. The broad line of faint dark EL contrast in Fig. 3(a) comes from the forward bias EL image and indicates the recombination activity of the grain boundary. This is much more pronounced in the EBIC image of the sample in Fig. 3(b), showing a strong recombination activity of the grain boundary at which the breakdown sites are found. The area, being highlighted by the dotted blue rectangle in Figs. 3(a) and 3(b), is displayed

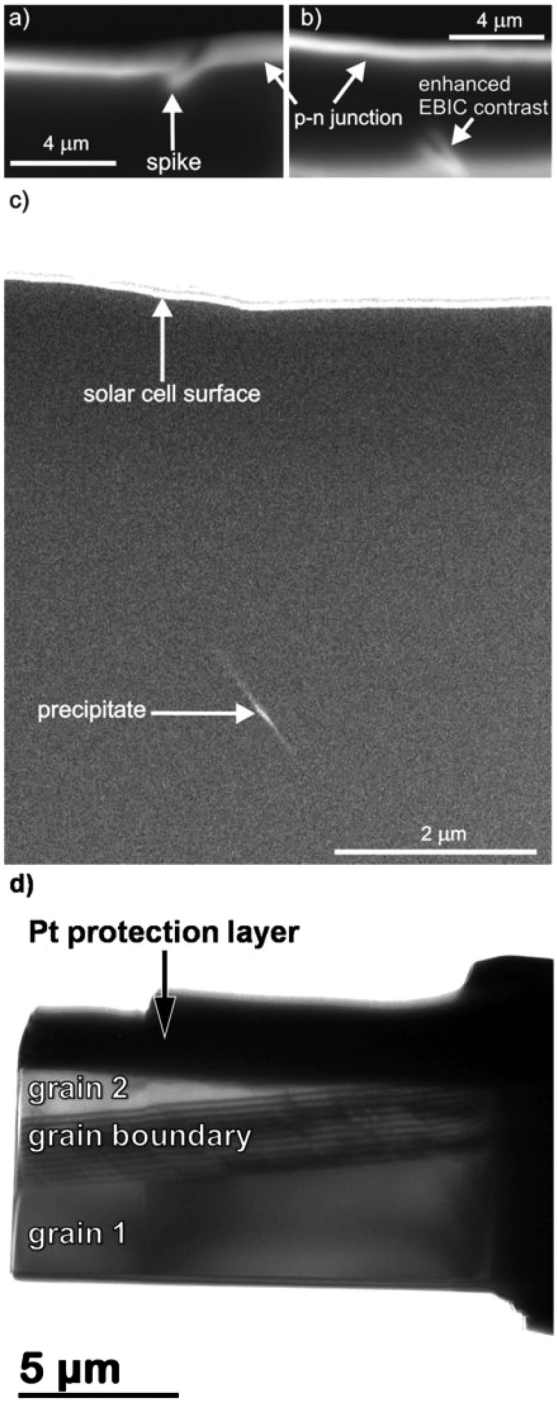

FIG. 2. (a) EBIC image of the front side FIB cut of sample 1 showing a spike in the p-n junction of a charge collecting structure, (b) EBIC image of the reverse side FIB cut of sample 1 revealing an enhanced EBIC signal about 4 μm deeper in the sample. The lamella is 1 μm thick. In (c), the SE material contrast of a rod-shaped precipitate on the reverse side of the lamella is shown after milling. (Image (c) was taken after the sample was attached to a TEM grid.) In (d), a TEM image of the 400 nm-thick FIB lamella is shown. (As in (a)-(c) the solar cell surface is on the top.)

in the high-resolution μ-ReBEL image in Fig. 3(c). It shows the breakdown site position at a micrometer scale, which allows the preparation of a FIB lamella at this breakdown site (the GB is indicated here by the solid (blue) lines serving as guides to the eye). This time the FIB lamella was prepared planar (i.e., parallel to the surface of the solar cell sample)

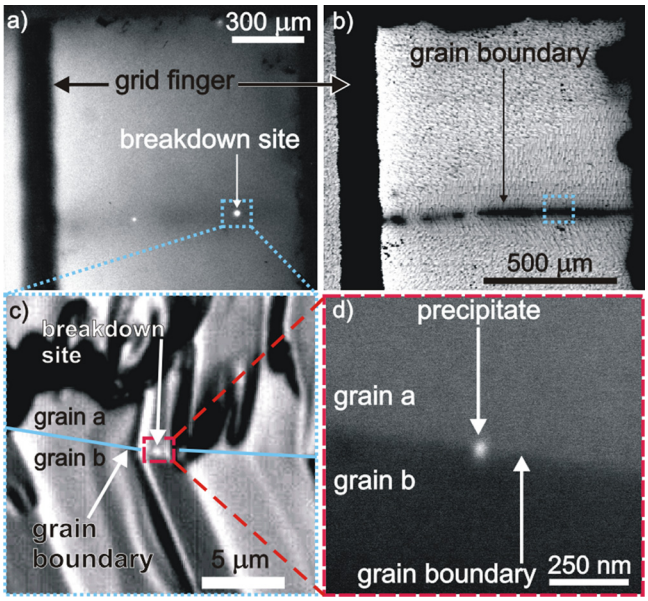

FIG. 3. (a) Overlay of a forward EL image at 601 mV and μ-ReBEL image at -10 V showing a faint line of recombination EL contrast and two breakdown sites on this line, (b) EBIC image taken at 30 keV revealing the strong recombination activity of the GB. In (c), a high resolution μ-ReBEL image (at -10 V) of the breakdown site marked by a dotted blue rectangle in (b) is shown. At the red dashed rectangle, a planar FIB preparation was performed, and in (d), a SEM image of the FIB sample shows strong material contrast at the breakdown site position and reveals the two grains as well.

from the area highlighted by the dashed red rectangle in Fig. 3(c).

The planar preparation enables a very good spatial correlation of the breakdown site and its root cause. Already, at an early stage of the FIB preparation, a SEM image of sample 2 shows a clear material contrast indicating a precipitate exactly at the breakdown site position as revealed in Fig. 3(d). Since the contrast component by backscattered electron channeling differs for various grain orientations, the different grains can be observed in the SEM image as well.

RESULTS OF THE STEM STUDY OF SAMPLE 1

The bright-field TEM image in Figure 4 shows the structure of the TEM lamella:

Two silicon grains adjoin by a large-angle boundary elongating through the whole specimen. In the electron microscope, the grain boundary was imaged by the typical extinction fringes, which are associated with the inclination of the boundary to the electron beam. The boundary fits the different orientations of the grains which have to be rotated by $\sim$129.5° around the $[\bar{1}\bar{1}0]$ axis in order to coincide crystallographically, whereas the $[\bar{1}\bar{1}0]$ axis is common for both grains. Crystallographic analyses revealed the grain boundary plane to be parallel to $(\bar{1}1\bar{3})$ of the right grain (grain 1) and to $(\bar{1}13)$ of the left grain (grain 2), and furthermore characterized the boundary plane as mirror. That typifies the boundary to be originally a symmetrical tilt boundary of the specifics $[\bar{1}\bar{1}0](\bar{1}1\bar{3})$ Σ11. However, processes of both grain growth and reactions with gliding dislocations distinctly modified the structure of the boundary. Thus, a deeper look into the structural details (see, Fig. 5) demonstrates a high

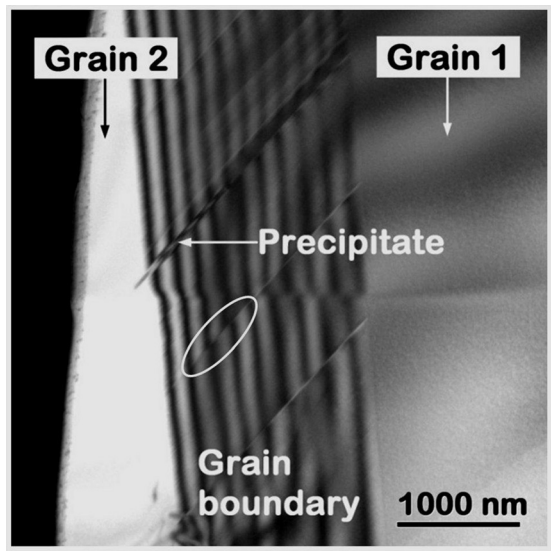

FIG. 4. TEM bright-field image demonstrating the microstructure of the mc Si in the region of interest, which has been specified as prebreakdown active. The oval marks shifts in the extinction lines caused by a defect crossing the boundary.

number of fault planes with a distance of 2-5 nm appearing parallel to the $(\bar{1}13)$ plane of grain 2 and $(\bar{1}1\bar{3})$ of grain 1, which is consistent with the boundary plane. These fault planes are assumed to build up multiple steps in the boundary with terraces parallel to the boundary plane. Forming the terraces and steps, the boundary path inclined with respect to its original $(\bar{1}1\bar{3})$ plane. The diffraction pattern in Fig. 5 furthermore shows weak streaks in the direction perpendicular to the steps, which might demonstrate the existence of stacking faults (SFs). Their origin is assumed in the dissociation of gliding dislocations on {111} planes by reactions of those dislocations with the boundary. In numerous earlier studies, interactions between dislocations and boundaries were elucidated.[19–24] For moving dislocations, even the highly symmetric Σ3 twin boundaries cannot be overcome by simple penetration. In general, the processes have been found to be very complex involving absorption, dissociation, recombination, and emission of dislocations.[22] All these processes consume energy and thus increase the energy of the boundary, which favours heterogeneous precipitation.

In the case of our specimen, there are indeed hints to reactions between dislocations and the boundary: In-between the multiple steps, distinct stripe defects were found in the boundary, which change the orientation of the silicon much more than the neighboring steps. That is illustrated by the corresponding breaks in the extinction fringes of the boundary in Figure 5 as well as in Figure 4 (cf., the oval marks). It appears that one of these defects induced the precipitation of a rod-like particle, which elongates along about one third of the defect line, as illustrated in the diagonal of the bright-field image. Another particularity can be seen in the enlarged cutout in Figure 5: It consists of a very rough defect path adjacent to the precipitate, which might be caused by the silicide-forming processes.

Some structural characteristics of the precipitate are demonstrated by the TEM-images of Figure 6: On the right, a TEM bright-field image illustrates the parallel orientation of

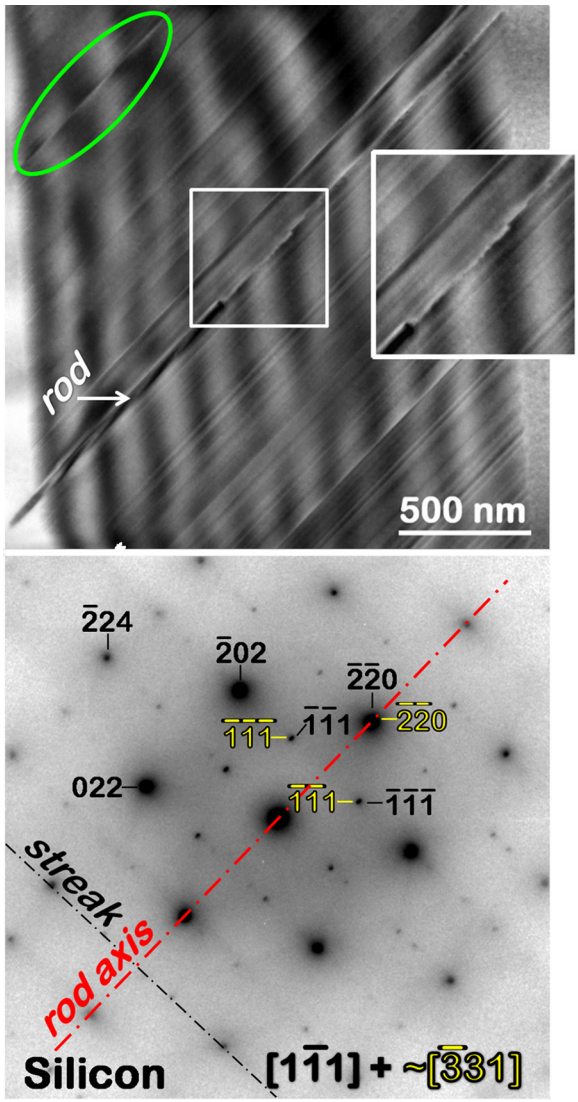

FIG. 5. TEM bright-field image of the grain boundary (above) and the corresponding selected area diffraction pattern (below), which was contrast-inverted for a clear demonstration of the particularities (such as: the reflections of Bragg diffraction in both, Si-grain 1 in $[1\bar{1}1]$ orientation, and Si-grain 2 in ~$[\bar{3}31]$ orientation, as well as of double diffraction in Si-grain 2, and, finally, weak streaks caused by occasional stacking faults). The axis of the precipitated rod has been marked in the diffraction pattern to illustrate its relative orientation to the silicon grains. The enlarged inset demonstrates the rough defect line next to the particle head, whereas the oval again marks shifts in a extinction lines caused by the defect crossing the boundary.

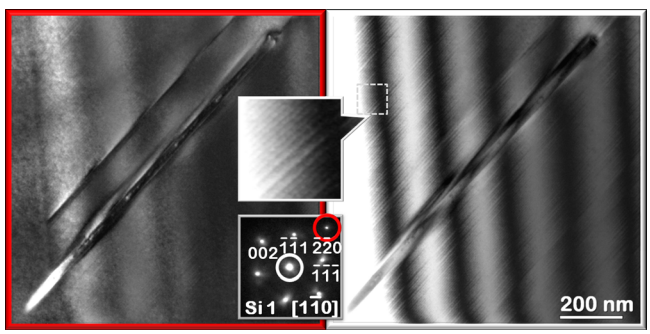

FIG. 6. Comparison of TEM bright-field (right) and TEM dark-field (left) of the grain boundary region with the precipitate (i.e., either transmitted beam, or $(\bar{2}\bar{2}0)$ reflection of grain 1 being selected, as illustrated by the diffraction pattern). The second inset is a magnified cut out from the bright-field image and shows stripe defects caused by steps in the boundary.

the rod axis in relation to the steps in the boundary, which are magnified in the inset. On the left, the specialty of the above discussed stripe defects as preferential precipitation sites is emphasized: In $(\bar{2}\bar{2}0)$ dark-field conditions (with grain 1 in $[1\bar{1}0]$ orientation), the steps became extinct and only the stripe defects, as well as the particle appeared in the silicon grain boundary. Obviously, the rod was precipitated at the stripe defect running along the diagonal of the image. Furthermore, the projection geometry of the rod with its exit face sticking out of the sample surface (located in the left lower corners) allowed estimating both, a 7.5° inclination of the rod with respect to the surface of the TEM lamella and a rod size of 30 nm in diameter and 1200 nm in length (whereas the length was limited by cutting during the FIB preparation). The precipitate additionally shows periodically aligned defects, which might be caused by the misfit to the silicon matrix.

The dark field conditions of the left pane of Figure 7 correspond to two-beam imaging conditions with the excited $(\bar{2}02)$ reflection of the left grain (grain 2). That allows identifying the above mentioned stripe defects as straight dislocations in the grain boundary, which appeared on $(\bar{1}11)$ planes of grain 2 with the dislocation lines being parallel oriented to $[\bar{1}\bar{1}0]$. Note the contrast oscillations around the lines, they show the inclination of the dislocations with respect to the sample surface. The source of the dislocations cannot be determined–they might have been originated from grain boundary movement during grain growth but might also have been moved from the grain interior into the boundary to react and split into partials there. Those parts, finally remaining in the boundary, appear to be preferential precipitation sites, setting the focus of any precipitation study onto the details of the dislocation reactions, which are not yet fully understood.

The middle picture of Figure 7 shows the magnified region around the rod-like particle, where the chemical composition was investigated by EDXS. A typical cutout of this region is marked by the white rectangle in the image and characterized by the corresponding EDX-intensity maps on the right. The maps clearly show that the rod consists of iron and silicon. In addition, EDX-measurements across the precipitate revealed that the small oxygen signal stays constant as in the surrounding of the rod. That is consistent with the formation of an iron silicide. The particular crystallography of the rod was identified by NBED.

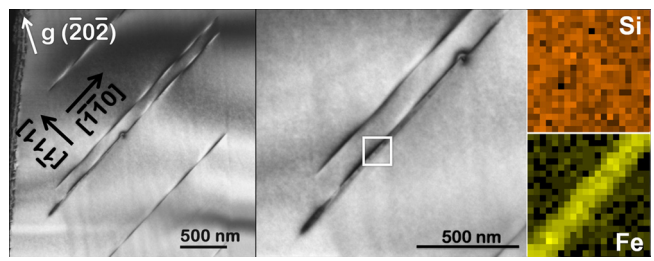

FIG. 7. Precipitation of an iron-silicon compound at one of a number of dislocations on $(\bar{1}11)$ planes (grain 2) with their lines being parallel to $[\bar{1}\bar{1}0]$, which reacted with the boundary. Outer left pane: Two-beam image with the excited $(\bar{2}02)$ reflection of the left grain (grain 2); Middle pane: Rod-like precipitate following the line of a dislocation; Outer right pane: EDX-intensity maps of the silicon-Kα and iron-Kα signals of the field marked in the middle pane.

By tilting cycles in the electron microscope and identification of the NBED patterns, the precipitate could be attributed to α-$FeSi_2$, which crystallizes in a tetragonal cell (space group P4/mmm with a = 2.68 Å and c = 5.13 Å).[25] It is characterized by a range of homogeneity limited at 1320 K to silicon content from 69.5 (x = 0.13) to 72.3 (x = 0.23) atomic percent, which is related to a large number of equilibrium structural vacancies in the iron sublattice and a complete silicon sublattice.

As demonstrated by Figure 8, the α-$FeSi_2$ precipitate was grown in a characteristic manner in relation to the silicon matrix. On the left pane, the STEM image of the precipitate is plotted together with diffraction patterns of the silicide and the silicon grain 2. The NBED patterns clearly explain both the orientation relationships between the silicide and the surrounding silicon grains, and the orientation of the rod axis. As deduced from the rod arrangement to the upper diffraction pattern, the rod axis is aligned along the [110] direction of the α-$FeSi_2$ implicating the main growth direction. Note that the NBED pattern of the precipitate consists of three classes of reflections: (i) the reflections of silicon grain 2 (the left silicon grain on Figures 4–7), (ii) those of the α-$FeSi_2$, and (iii) reflections which resulted from double diffraction in the adjacent silicon. Orienting the silicide with the [001] zone axis parallel to the electron beam simultaneously aligned the silicon grain 2 in ∼[1$\bar{1}$2] zone axis orientation, which implicates the precipitate/silicon orientation relationships (110) α-$FeSi_2$ II ($\bar{2}\bar{2}$0) Si and (1$\bar{1}$0) α-$FeSi_2$ II ∼ ($\bar{1}$11) Si, and confirms results of earlier investigations.[15] Please note that the [$\bar{1}\bar{1}$0] axis (and thus, the ($\bar{2}\bar{2}$0) plane) is common for both silicon grains located above and below the grain boundary. That

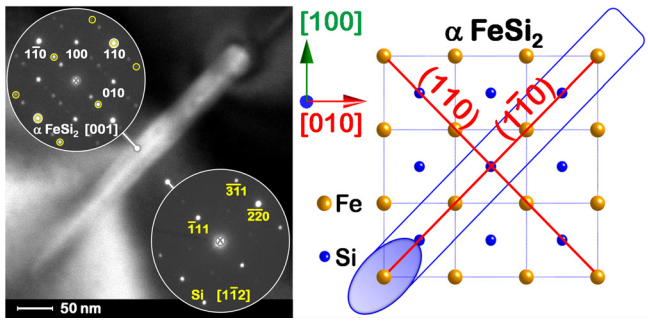

FIG. 8. Attribution of the rod to α $FeSi_2$ by NBED. Left pane: STEM-image of the precipitate with the corresponding NBED patterns of α-$FeSi_2$ in [001] orientation and of silicon grain 2 in ∼[1$\bar{1}$2] orientation; Right pane: Illustration of the specific rod orientation.

indicates a general arrangement of the (110) plane of α-$FeSi_2$ parallel to a plane of the {220} family of Si, the plane distances of which match with a small difference of 0.81% at room temperature and becomes only 0.03% at 1073 K.[26] Thus, the (110) planes grew fastest, yielding the rod-like shape with the elongation in the [110] direction and the corresponding relationship to the silicon, which is shown on Figure 8.

RESULTS OF THE STEM STUDY OF SAMPLE 2

As predicted by SEM during the FIB preparation of the second sample (see, Fig. 2), a precipitate was found exactly at the breakdown site in sample 2 by STEM investigations. A HAADF-STEM image of the precipitate is shown on the main pane of Fig. 9. The brightness of the particle is much

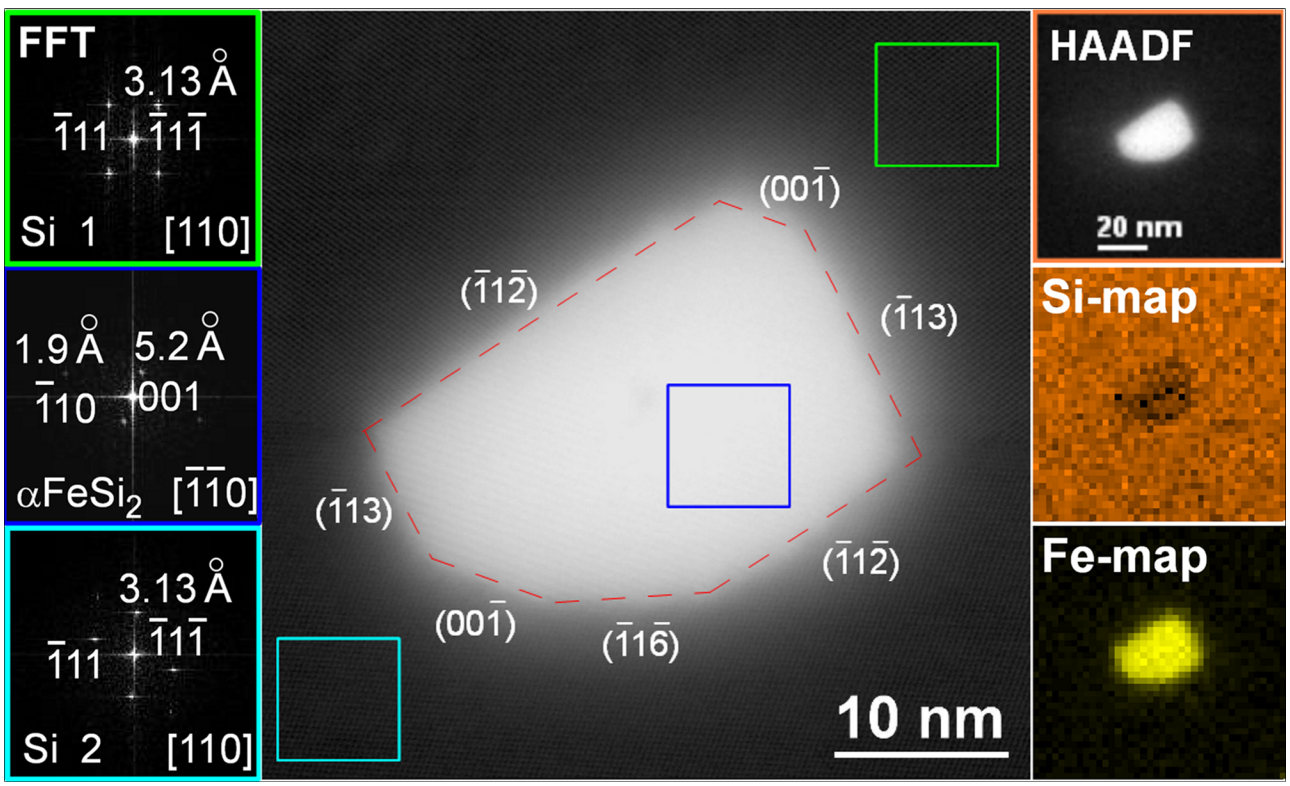

FIG. 9. HAADF-image of the iron silicide particle at the breakdown site in sample 2. Note the precipitation at a grain boundary. Right panes: STEM-image of the precipitate with the related EDX-intensity maps of the Si-Kα and Fe-Kα signals; Left panes: FFTs of the regions marked in the HAADF-image.

higher than that of the embedding silicon grains, which indicates a high average atomic number within the particle. As shown on the right side of Fig. 9, EDX-intensity maps of the Si-Kα and Fe-Kα signals indeed demonstrate the formation of an iron-silicon compound.

On the left side of Fig. 9, three fast Fourier transform (FFT)-images of regions, which are marked in the silicon grains and the precipitate in the HAADF-image, are shown. Please note that the middle FFT-image from the precipitate reveals reflections being related to a plane distance of 0.52 nm, which can be clearly attributed to the (001) plane of α-type $FeSi_2$. The second reflection corresponds to the $(\bar{1}10)$ plane distance and identifies the $[\bar{1}\bar{1}0]$ orientation of the α-type $FeSi_2$ particle. At the same time, both silicon grains (illustrated by the FFTs lying above (grain1) and below (grain 2) the FFT of the particle) are [110]-oriented with a rotation of 31.6° around the [110] direction pointing out of the paper plane. That corresponds to the orientation relationships between α-$FeSi_2$ and Si observed in the first sample: In both cases, the (110) plane of α-$FeSi_2$ grows parallel to a plane of the {220} family of Si. Moreover, the diameter of the precipitate of about 30 nm is consistent with that of the silicide rod in sample 1. The facets which are attributed to the polygonal shape of the particle are noted in Figure 9. A further agreement to sample 1 concerns the location of precipitation, which is a large-angle tilt boundary. However, in contrast to the [110] Σ 11 boundary in sample 1, in sample 2, a [110] Σ 27 boundary with $\theta \sim 31.6°$ was identified. The peculiarity of the atomic structure of the boundary is demonstrated on Fig. 10.

The annular dark-field STEM-image projects the columns of Si-atoms of the interfacial region along $[\bar{1}\bar{1}0]$ onto the paper plane. As already revealed by the FFTs in Fig. 9, the [110]-oriented grains above and below are rotated by $\theta \sim 31.6°$, which corresponds to a [110] Σ 27 boundary. However, there are modifications from this original boundary type yielding the formation of triangular twins, which are limited by [110] Σ 3 and [110] Σ 9 boundaries, as well as by complexes of SFs and dislocations. The detailed structure of the boundaries, which join the left triangular-shaped twin in Fig. 10 to the neighbored Si grains, is characterized in Fig. 11. Here, the structural units of the corresponding boundary types are illustrated schematically according to Refs. 19 and 27. In the [110] Σ 9 type boundary, rings of five and seven silicon atoms are configured in $[\bar{1}14]$ direction (of the upper grain), whereas the [110] Σ 3 type consists of rings of six silicon atoms lined up in $[1\bar{1}\bar{2}]$ direction (of the lower grain). In contrast, on the left side, a combination of stacking faults and dislocations joins the twin to the upper silicon grain. Dislocation cores are assumed to be arranged at the ends of the stacking faults, as well as at the crossing points of the different boundaries and are hardly to localize, as several defects are overlapping. However, the complexes of stacking faults and dislocations at the short side of the twin-triangle might indicate dislocation-boundary reactions, yielding a dissociation of the dislocations.

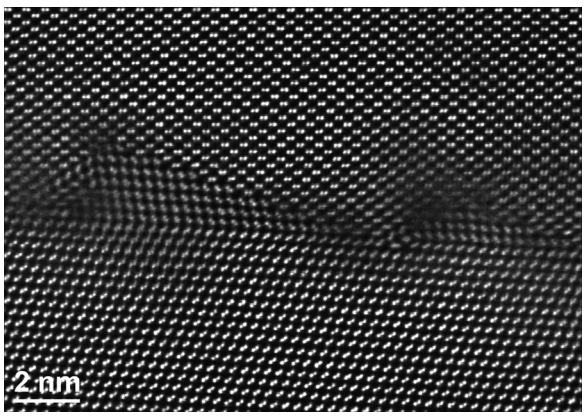

FIG. 10. HAADF-image of the [110] Σ 27 boundary, which is peculiarly terraced by the formation of triangular twins being limited by [110] Σ 3 and [110] Σ 9 boundaries as well as by complexes of SF and dislocations.

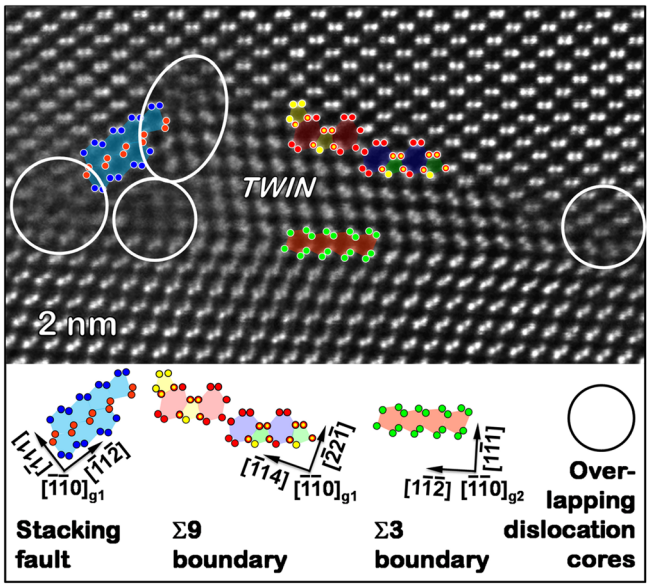

FIG. 11. Magnified cut out of the HAADF-image in Figure 10 demonstrating the detailed atomic structure of the boundaries of the triangular twins in the [110] Σ 27 boundary.

Although the exact location of the precipitation could not be specified in the second sample, there is a strong analogy with the findings in the first sample, where the silicide elongated along a dislocation line in the boundary. In a general sense, in both samples, particles of iron silicide precipitated at terraced large-angle tilt boundaries.

The additional NBED phase analysis of the precipitate in sample 2 confirms the preferential orientation of $[\bar{1}\bar{1}0]$ α-$FeSi_2$ parallel to [110] Si (cf., Figure 12). In spite of the beam diameter of about 3 nm, the NBED-pattern from the silicide consists of three overlaid parts: two diffraction patterns of the neighboring silicon grains in [110]-orientation and one pattern attributed to α-$FeSi_2$ in $[\bar{1}\bar{1}0]$-orientation. That indicates two peculiarities, which yield the nano-beam was scattered not only in the silicide but also in the underlying Si-grains: a heterogeneous diameter of the $FeSi_2$ particle as implied by Figure 8, and a local incline of the silicon grain boundary below the silicide particle. Another interesting detail is revealed by a comparison of the NBED pattern in Figure 12 with the FFT-image of the particle in Figure 9, the HAADF-image of which was obtained before the NBED

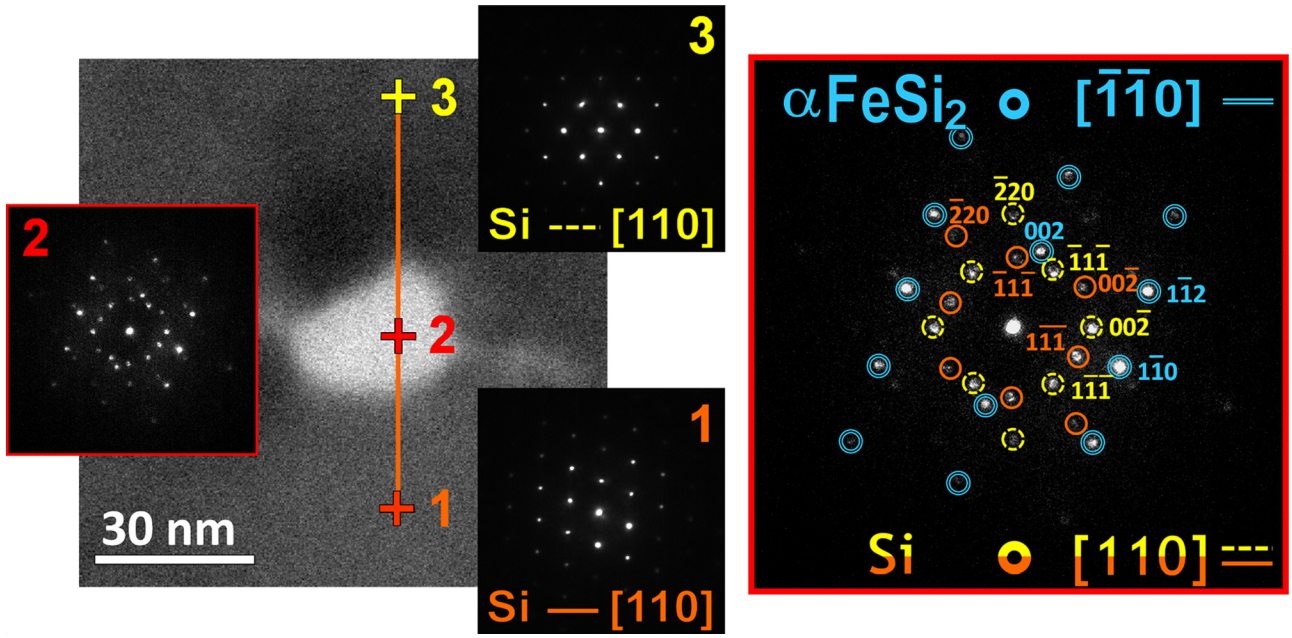

FIG. 12. Attribution of the precipitate to α-$FeSi_2$ (distorted CsCl-type) by NBED. Left pane: STEM-image of the precipitate with the corresponding NBED patterns. Right pane: NBED pattern of the particle with the overlaid marks in orange, yellow, and blue, which belong to the silicon grain 1, silicon grain 2, and the α-$FeSi_2$ particle, respectively.

investigation. The extinction of {001}-$FeSi_2$ reflections in the NBED-pattern suggests an electron-beam induced phase transformation of the α-type $FeSi_2$ into a distorted CsCl-type $FeSi_2$ as described in Ref. 28. This is caused by a recombination of Fe atoms with vacancies at (000.5) accompanied by a slight displacement of Si atoms. For transformations of iron silicide phases vacancies are especially important as differences in the atomic structure of the typical metastable phases (c-FeSi (CsCl-type), γ-$FeSi_2$ (CaF_2-type), α-type $FeSi_2$ (distorted CsCl-type)), and the P 4/mmm α-type $FeSi_2$ mainly consist in the geometry of vacancies at Fe sites. Also the phase transition from the α- to the β-modification (which corresponds to a distorted CaF_2-type) is obtained by relocating half of the atoms from the α-type (001) Fe-layer into the (001) interplanar regions suppressing every second (111) Fe-layer.[29]

MODEL OF DEFECT-INDUCED BREAKDOWN (TYPE-2) IN MC-SI SOLAR CELLS

The STEM investigation revealed a needle-like α-$FeSi_2$ particle at the position of the defect-induced breakdown site. According to the SEM observations during FIB preparation, the particle is at least some μm in length. The α-phase is the only quasi-metallic $FeSi_2$-phase,[30] hence this precipitate is highly conductive. It can be expected to yield a Schottky junction to the p-type base material, as most metal silicides do. Furthermore, it can be expected to yield an ohmic tunnel contact to the highly n-doped emitter, if the α-$FeSi_2$ needle also penetrates the emitter. This suggests modeling the breakdown behavior of the defect as already mentioned in Ref. 4 and shown in Figure 13.

Applying a reverse bias at the solar cell also biases this Schottky junction in reverse. The breakdown mechanism expected for a Schottky junction is thermionic field emission.[31] In comparison to a p-n junction, the breakdown voltage is significantly lower due to the lower barrier height, which is valid even for a plane Schottky junction. Radermacher *et al.*[32] reported a barrier height of 0.84 eV for α-$FeSi_2$ on n-Si. Since the barrier heights to n- and to p-Si roughly add-up to the band gap, for p-Si, a considerably lower barrier height can be expected. Moreover, at the end of the needle, the electric field is strongly enhanced by the tip-effect. Therefore, the expected breakdown site is just at the end of the needle, and the breakdown voltage is further reduced. The breakdown voltage should also depend on the remaining length of the silicide needle in the p-material and on the inclination of the silicide precipitate to the surface plane. This (and the possible existence of other type-2 breakdown mechanisms) explains the relatively low and scattered breakdown voltages observed for the type-2 breakdown sites.[4]

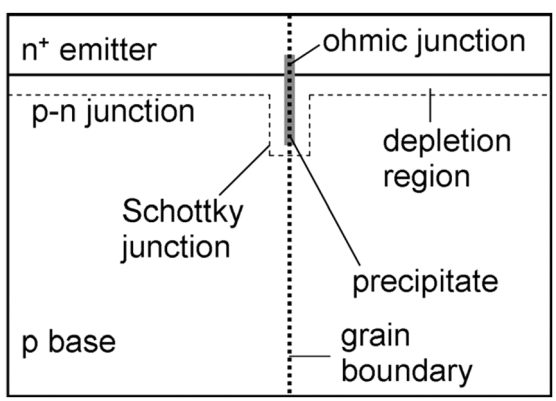

FIG. 13. Model of the precipitate-induced type-2 breakdown sites.[4] Figure reprinted with permission from O. Breitenstein, J. Appl. Phys. **109**, 071101 (2011). Copyright 2011 American Institute of Physics.

DISCUSSION AND CONCLUSION

This investigation has revealed that in two cases, the Fe-containing precipitates, lying in a grain boundary of the multicrystalline Si material and leading to defect-induced pre-breakdown, were needle-shaped α-type $FeSi_2$ precipitates showing well-defined orientation relations to the silicon. Their diameter was about 30 nm, but their length was found to be at least several μm. These findings correlate well with early TEM investigations on monocrystalline Si material[15,16] and with synchrotron-based XRF investigations on this material.[2,13] In sample 2, no μ-XRF investigations were done before, nevertheless the iron silicide precipitate was found. Since the breakdown site investigated here in detail behaved identical to a large number of other defect-induced (type-2) breakdown sites, we assume that this is a typical result. This would mean that, in present industrial mc solar cells, the defect-induced pre-breakdown is at least to a significant part due to Fe-contamination of the material. The α-$FeSi_2$ needles just have rarely been detected until now since they are so small (about 30 nm in diameter) that they are invisible in both, near-IR transmission light microscopy imaging (which is generally used for screening multicrystalline material for precipitates[33]) and conventional microanalysis techniques. Nevertheless, an influence of other metal precipitates cannot be excluded.

From the thermodynamic point of view, α-$FeSi_2$ is stable between 1220 °C and 915 °C and is probably formed at high temperature during silicon crystallization.[14,15] Thus, it is expected that the α-$FeSi_2$ needles, like the other precipitates regularly found in mc solar cells, exist already in the starting material and are not generated by the cell manufacturing process. Although the cell manufacturing process affects the α-$FeSi_2$ structure by succeeding thermal annealing, α-$FeSi_2$ can still be found in mc solar cells, which implies that the eutectoidal decomposition of α-$FeSi_2$ into the β-modification and silicon is slow at the respective temperatures.

Until now, the influence of iron in multicrystalline silicon solar cells has been discussed only with respect to its recombination behavior.[13] The Schottky-type breakdown mechanism proposed here significantly differs from the various types of avalanche breakdown sites introduced in Refs. 3 and 5. In the avalanche cases, it is the p-n junction, which breaks down. Its breakdown voltage is just reduced, for a base doping concentration of $10^{16}\,cm^{-3}$, from the value for a plane junction of about 60 V down to 13 V for a bowl-shaped geometry with a radius of 300 nm,[34] which is about the junction depth. Hence, for this base doping concentration, avalanche breakdown at voltages below 13 V is not expected to occur. The type-2 breakdown, however, appears in this material already at significantly lower reverse bias.[4,6] For alkaline textured solar cells, until now, there are no hints that there are any etch pits or preferred phosphorous diffusion in the sites of the $FeSi_2$-needles. However, even if in alkaline textured solar cells, there would be etch pits or preferred phosphorous diffusion in the sites of $FeSi_2$-needles, as in acidic etched cells, the lower barrier height at the silicide precipitates would cause Schottky breakdown in such a site at much lower reverse bias than expected for the avalanche breakdown. It can be expected that a similar breakdown mechanism is also active for type-2 breakdown caused by other precipitates.

In isotextured solar cells, precipitates (and, in particular, $FeSi_2$) could not be found at breakdown sites so far. Maybe the precipitates were etched away by the acidic texturization process keeping some Fe atoms over—enough Fe atoms to induce the breakdown behavior observed, but too few to be detected by analytical electron microscopy. We suppose that, if a line defect is sufficiently strong decorated, e.g., by iron, it may lead to the type-2 breakdown as described here, even if the TEM does not show any foreign phase. It is well known that Fe atoms create electronic levels in the gap. If the distance between neighboring impurity atoms is low enough, their electronic levels will overlap, leading to conduction by variable range hopping according to Mott's theory.[35] Hence, these atomically decorated line defects may act like the quasi metallic silicide rods, also leading to type-2 breakdown.

ACKNOWLEDGMENTS

This work was financially supported by the German Federal Ministry for the Environment, Nature Conservation and Nuclear Safety and by industry partners within the research cluster "SolarWinS" (Contract No. 0325270C). The content is the responsibility of the authors.

[1]D. Lausch, K. Petter, R. Bakowski, C. Czekalla, J. Lenzner, H. v. Wenckstern, and M. Grundmann, "Indentification of pre-breakdown mechanism of silicon solar cells at low reverse voltages," Appl. Phys. Lett. **97**, 073506 (2010).
[2]W. Kwapil, P. Gundel, M. C. Schubert, F. D. Heinz, W. Warta, E. R. Weber, A. Goetzberger, and G. Martinez-Criado, "Observation of metal precipitates at breakdown sites in multicrystalline silicon solar cells," Appl. Phys. Lett. **95**, 232113 (2009).
[3]J. Bauer, J.-M. Wagner, A. Lotnyk, H. Blumtritt, B. Lim, J. Schmidt, and O. Breitenstein, "Hot spots in multicrystalline silicon solar cells: Avalanche breakdown due to etch pits," Phys. Status Solidi RRL **3**, 40 (2009).
[4]O. Breitenstein, J. Bauer, K. Bothe, D. Lausch, U. Rau, J. Schmidt, M. Schneemann, M. C. Schubert, J.-M. Wagner, and W. Warta, "Understanding junction breakdown in multicrystalline solar cells," J. Appl. Phys. **109**, 071101 (2011).
[5]J. Bauer, D. Lausch, H. Blumtritt, N. Zakharov, and O. Breitenstein, "Avalanche breakdown in multicrystalline solar cells due to preferred phosphorous diffusion at extended defects," Prog. Photovoltaics (in press).
[6]W. Kwapil, M. Kasemann, P. Gundel, M. C. Schubert, W. Warta, P. Bronsveld, and G. Coletti, "Diode breakdown related to recombination active defects in block-cast multicrystalline silicon solar cells," J. Appl. Phys. **106**, 063530 (2009).
[7]J.-M. Wagner, J. Bauer, and O. Breitenstein, "Classification of pre-breakdown phenomena in multicrystalline silicon solar cells," in *24th Eur. Photovolt. Solar Energy Conf., Hamburg, Germany* (2009), pp. 925–929.
[8]R. Bakowski, R. Lanzsch, T. Kaden, K. G. Eller, D. Lausch, Y. Ludwig, and K. Petter, "Comparison of recombination active defects in multicrystalline silicon by means of photoluminescence imaging and reverse biased electroluminescence," in *26th Eur. Photovolt. Solar Energy Conference, Hamburg, Germany* (2011), pp. 1839–1842.
[9]T. U. Nærland, L. Arnberg, and A. Holt, "Origin of the low carrier lifetime edge zone in multicrystalline PV silicon," Prog. Photovoltaics **17**, 289 (2009).
[10]J. Chen, T. Sekiguchi, D. Yang, F. Yin, K. Kido, and S. Tsurekawa, "Electron-beam-induced current study of grain boundaries in multicrystalline silicon," J. Appl. Phys. **96**, 5490 (2004).
[11]V. Kveder, M. Kittler, and W. Schröter, "Recombination activity of contaminated dislocations in silicon: A model describing electron-beam-induced current contrast behavior," Phys. Rev. B **63**, 115208 (2001).
[12]D. Lausch, K. Petter, R. Bakowskie, J. Bauer, O. Breitenstein, and C. Hagendorf, "Classification and investigation of recombination-active

defect structures in multicrystalline silicon solar cells," in *Proceedings of the 27th EUPVSEC, 2012, Frankfurt (Main), Germany* (2012).
[13]T. Buonassisi, A. A. Istratov, M. Heuer, M.A. Marcus, R. Jonczyk, J. Isenberg, B. Lai, Z. Cai, S. Heald, W. Warta, R. Schindler, G. Willeke, and E. R. Weber, "Synchrotron-based investigations of the nature and impact of iron contamination in multicrystalline silicon solar cells," J. Appl. Phys. **97**, 074901 (2005).
[14]M. Seibt, R. Khali, V. Kveder, and W. Schröter, "Electronic states at dislocations and metal silicide precipitates in crystalline silicon and their role in solar cell materials," Appl. Phys. A **96**, 235 (2009).
[15]A. G. Cullis and L. E. Katz, "Electron microscope study of electrically active impurity precipitate defects in silicon," Philos. Mag. **30**, 1419 (1974).
[16]P. D. Augustus, J. Knights, and L. W. Kennedy, "A correlation between the electrical breakdown of silicon bipolar transistors and impurity precipitates," J. Microsc. **118**, 315–320 (1980).
[17]M. A. Falkenberg, H. Schuhmann, M. Seibt, and V. Radisch, "Localization and preparation of recombination-active extended defects for transmission electron microscopy analysis," Rev. Sci. Instrum. **81**, 063705 (2010).
[18]D. Lausch, K. Petter, H. v. Wenckstern, and M. Grundmann, "Correlation of pre-breakdown sites and bulk defects in multicrystalline silicon solar cells," Phys. Status Solidi RRL **3**, 70–72 (2009).
[19]L. Priester, J. Thibault, and V. Pontikis, "Theoretical, numerical, and experimental approaches for structural studies of grain boundaries: Methods, remarkable results and perspectives," Solid State Phenom. **59–60**, 1–50 (1998).
[20]G. Saada, "Stress field at interfaces," Solid State Phenom. **59–60**, 77–98 (1998).
[21]S. Hagège and Y. Champion, "Dislocations, steps and heterophase interfaces," Solid State Phenom. **59–60**, 63–76 (1998).
[22]C. Solenthaler, "On dislocation reactions in F.C.C. Σ3 twin boundaries," Mater. Sci. Eng. A **125**, 57–66 (1990).
[23]C. Solenthaler, "Reactions between crystal dislocations and grain boundary dislocations in near-coincidence boundaries," Mater. Sci. Eng. A **113**, 95–119 (1989).
[24]H. Wang, N. Usami, K. Fujiwara, K. Kutsukake, and N. Nakajima, "Microstructures of Si multicrystals and their impact on minority carrier diffusion length," Acta Mater. **57**, 3268–3276 (2009).
[25]F. A. Sidorenko., V. Gel'd, V. Ya. El'ner, and B. V. Ryzhenko, "Investigation of multiparticle atomic correlations in α-$Fe_{1-x}Si_2$ by Mössbauer spectroscopy," J. Phys. Chem. Solids **43**, 297–303 (1982).
[26]C. Detavernier, C. Lavoie, J. Jordan-Sweet, and A. S. Özcan, "Texture of tetragonal α-$FeSi_2$ films on Si (001)," Phys. Rev. B **69**, 174106 (2004).
[27]J. Thibeault, J.-L. Putaux, A. Jacques, and A. George, "Structure and characterization of dislocations in tilt grain boundaries between Σ1 and Σ3: A high-resolution electron microscopy study," Mater. Sci. Eng. A **164**, 93–100 (1993).
[28]M. Naito, M. Ishimaru, J. A. Valdez, and K. E. Sickafus, "Electron-irradiation induced phase transformation in α-$FeSi_2$," J. Appl. Phys. **104**, 073524 (2008).
[29]N. Jedrecy, A. Waldhauer, M. Sauvage-Simkin, R. Pinchaux, and Z. Zheng, "Structural characterization of epitaxial α-derived $FeSi_2$ on Si (111)," Phys. Rev. B **49**, 4725–4732 (1994).
[30]T. Hirano and M. Kaise, "Electrical resistivities of single-crystalline transition-metal disilicides," J. Appl. Phys. **68**, 627 (1990).
[31]E. H. Rhoderick and R. H. Williams, *Metal—Semiconductor Contacts* (Clarendon, Oxford, 1988).
[32]K. Radermacher, S. Mantl, Ch. Diecker, and H. Luth, "Ion beam synthesis of buried α-$FeSi_2$ and β-$FeSi_2$ layers," Appl. Phys. Lett. **59**, 2145–2147 (1991).
[33]J. P. Rakotoniaina, O. Breitenstein, M. Werner, M. H. Al-Rifai, T. Buonassisi, M. D. Pickett, M. Ghosh, A. Müller, and N. Le Quang, "Distribution and formation of silicon carbide and silicon nitride precipitates in block-cast multicrystalline silicon," in *20th Eur. Photovolt. Solar Energy Conf., Barcelona, Spain* (2005), pp. 773–776.
[34]S. M. Sze and G. Gibbons, "Effect of junction curvature on breakdown voltage in semiconductors," Solid-State Electron. **9**, 831 (1966).
[35]N. F. Mott, *Metal-Insulator Transitions* (Taylor & Francis, London 1990).